Study of Three WFS for the Modular System in a Portable AO Instrument: ALIOLI

Esther Soria[1,2][a] and Roberto López[1,2][b]

[1]*Instituto de Astrofísica de Canarias, C/Vía Láctea s/n, La Laguna, E-38205, Spain*

[2]*Departamento de Astrofísica, Universidad de La Laguna, La Laguna, E-38200, Spain*

Keywords: Adaptive Optics, High Resolution, Wavefront Sensor, Wavefront Corrector, Medium Sized Telescopes.

Abstract: Adaptive optics (AO) systems correct atmospheric turbulence in real time and they are normally designed for large telescopes but not for modest due to their cost. In this paper, we propose a portable AO instrument, named ALIOLI, capable of be installed in different medium and small-sized telescopes. The novelty of this new instrument is the modularization of its components which allows great flexibility in the design, being possible easily adapt the instrument to the working telescope or observing technique by adjusting each module independently. Here we present the instrument concept and a preliminary design for its installation in the Carlos Sanchez Telescope (⊘ 1.5m, Teide Observatory (Canary Islands)). The Wavefront Sensor (WFS) module is intended to be used with three different WS, Shack-Hartmann, Two Pupil Plane Position and non-modulated Pyramidal, allowing a joint configuration for comparative studies. A comparison of the response of these sensors has been carried out by simulating the instrument in Python. The simulation results demonstrate the goodness of the applied algorithms and the higher linearity and precision of the SH WFS in comparison with the others two.

1 INTRODUCTION

The wavefront (WF) of light coming from a distant source such as an astronomical object can be considered flat when it propagates through the void. However, when this WF cross through the turbulent and variable atmosphere, it is distorted due to fluctuations in the refractive index and the result is a blur in the image of the object that is being observed (Hickson, 2014).

Adaptive optics (AO) is a technique that characterizes and corrects atmospheric turbulence in real time using a Wavefront Sensor (WFS). The WFS must measure the incoming wavefront to allow the correction with an active element, located along the optical path, being the most common a Deformable Mirror (DM). The wavefront reconstructor is in charge of translating the wavefront signal into DM language.

The construction of large telescopes requires the development of increasingly sensitive and faster Adaptive Optics systems, leaving behind the large number of telescopes, smaller and still crucial in many observation campaigns. Therefore, improving the spatial resolution would open the possibility of equipping them with scientific instrumentation such as an spectrograph or coronagraph, which multiplies observers' options.

It is in this context that the concept of ALIOLI emerges. This is an evolution of AOLI instrument (Adaptive Optics and Lucky Imager) (Colodro-Conde and others., 2018) towards a Lightweight Instrument customised for small telescopes, constituting a thesis project. For this approach, the LI was put aside and the main effort is concentrated on selecting the most appropriate WFS, as well as on undertaking a study of the behaviours of different WFS approaches depending on the telescope, the atmospheric conditions or even the science instrument we work with.

As a WF propagates, it is possible to predict the WF geometry using ray optics because the light at each point in the WF travels perpendicularly to that point. We wish to determine the shape of the incoming WF, thus if we divide the WF surface into area differentials, we could know the slope distribution measuring the mean slope in each zone. This linear relationship between beam slopes and light displacement underlies most wavefront sensing techniques, and it is the underlying principle of operation of the 3 sen-

[a] https://orcid.org/0000-0003-2486-7998
[b] https://orcid.org/0000-0002-6491-5555

Soria, E. and López, R.
Study of Three WFS for the Modular System in a Portable AO Instrument: ALIOLI.
DOI: 10.5220/0010778000003121
In *Proceedings of the 10th International Conference on Photonics, Optics and Laser Technology (PHOTOPTICS 2022)*, pages 17-25
ISBN: 978-989-758-554-8; ISSN: 2184-4364

sors with which we are going to work, the Shack-Hartmann (S-H,) the Two Pupil Plane (TP3) and the non-modulated Pyramidal (nm-PYR).

A wavefront sensor uses optical elements to transform readable intensity distribution on a detector into wavefront deformations. It consists in a hardware part, the optical elements and the detector, and a software part, the signal processing. The computation must be fast enough, which means, practically, that only linear reconstructors are useful. A linear reconstructor typically performs matrix multiplication.

The S-H WFS was developed in the late 1960s, evolving from the Hartmann screen test (Thibos, 2000). It works by subdividing the complex field in the plane of the telescope's pupil, the hardware part is a lenslet array that generates low resolution images of the object. See figure 1. The integrated gradient of the wavefront across the lenslet is proportional to the displacement of the centroid (dx,dy). Consequently, any phase aberration can be approximated by a set of discrete tilts.

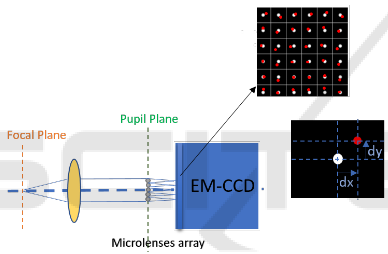

Figure 1: Shack-Hartmann WFS scheme.

The nm-PYR WFS was first introduced in 1996 by Ragazzoni (Ragazzoni, 1996). For this sensor the hardware part is a pyramid, which is placed on the focal plane of the telescope and the light is focused on the apex of the pyramid. This element subdivides the focal plane of the telescope into four quadrants. The output of the prism is collimated obtaining four aperture images in the focal plane of the lens. From the intensity distribution in the four pupils we can calculate local slopes.

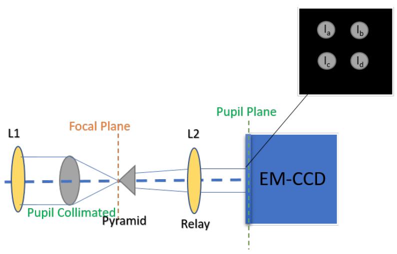

Figure 2: Pyramid WFS scheme.

The TP3 WFS was conceived by van Dam and Lane in 2002, and was first used in a closed-loop AO system in 2017 (Colodro-Conde and others., 2017). It is based on the derivation of the wavefront aberrations from two defocused intensity images (van Dam and Lane, 2002). For this sensor the hardware part will be an optical element which generates an optical path difference. It working principle is based on the divergences and convergences of the rays in an aberrated WF, which create fluctuations intensity maps. The total intensity must be constant between the ray path due to the principle of conservation of energy. Thus, an area of light divergent in one image will have the same total intensity as its respective convergent area in the other image. The ray tracing is performed by measuring the displacement of the corresponding light and dark regions in the defocused images, see figure 3.

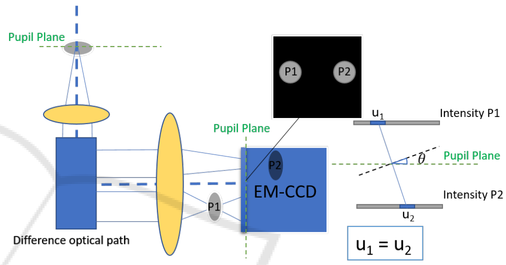

Figure 3: Two Pupil Plane WFS scheme.

This paper presents the first work carried out to determine the best WFS to couple ALIOLI to different scientific instruments in medium-sized telescopes. The final purpose is to develop simulations, laboratory tests and telescopic operation of a prototype that offers the possibility of using one type or another according to the observing conditions.

2 MODULAR CONCEPT

The ultimate purpose of this project is to have a portable instrument that could be mated and removed in different telescopes. For this reason, a modular system has been proposed. The modules in the ALIOLI instrument are as follows:

- Telescope Simulator. An optical fiber has been used as a reference star. This block has been initially developed for the TCS. To simulate the TCS aperture, two achromatic doublets and a physical pupil have been used. See Figure 4 blue beam.
- Wavefront Corrector. This block consisting of a DM placed on the conjugated pupil plane of the telescope that act as a phase modulator. It was decided for the simplest design using commercial achromatic doublets. The collimating lens images

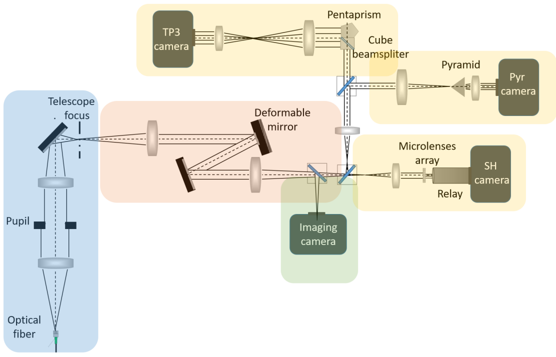

Figure 4: Mounting proposals for each module of the ALIOLI instrument.

the entrance pupil on the DM, and a second lens refocuses the object. The DM is an ALPAO device with 88 actuators and a pupil diameter of 20mm. This compact design will allow to incorporate a Tip Tilt Mirror (TTM) along the optical path, but due to the tip/tilt stroke of this DM is $40\mu m$, in the actual design the tip-tilt corrections could be assumed by the DM. See Figure 4 red beam.

- Wavefront Sensor. A WFS with interchangeable S-H, TP3, PYR modules. The optical design for each wavefront is done and it is widely reported in Section 3. The sensor camera, an Andor Ixon DU-897 camera, which is based on a sub-photon noise 512x512 e2v EMCCD (Electron Multiplying Charge-Coupled Device) detector, and the collimating lenses are common for the three approaches. See Figure 4 yellow beam. Each WFS carries an image analysis program for calculating the slopes, Slopes Calculation Program (SCP), that reproduce the incident wavefront.
- Control Software. The same modular strategy has been proposed for the Control Software. See Figure 5. Here, we will distinguish three modules. The first one is the Frame Grabbing Software (FGS) whose objective is to continuously acquire images from the WFS camera, the input data, using an appropriate configuration depending on the post processing. This part send the images to the next level. The second ones is the Slope Calculation Program (SCP) which receives the images and processes them according to each algorithm. The information collected after processing is sent in terms of slopes or Zernike coefficients to the next level. The last module is the Control Loop Program (CLP). The base of this prototype is to use resources of previous projects, so the CLP used is the one developed for AOLI, whose description is widely reported in (Colodro-Conde and others., 2017).

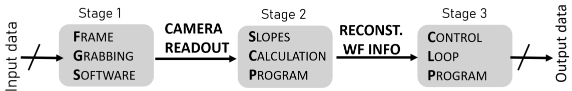

Figure 5: Pipeline for the Analysis + Control Software.

- Graphics Manager. A python application has been developed to manage the graphics produced during the AO process, such as the reconstruction of the wavefront, the DM geometry or the WFS camera readout. This application allows view real-time information relevant to the sensing and close loop process, as well as save the information in the appropriate format.
- A Science System: the initial approach is to place directly an imaging camera. Since our WFC maintains the telescope's F#, we have decided to attach the lenses of FastCam instrument, based on Lucky Imaging technique, (Alejandro Oscoz, 2008) to our science arm. See Figure 4 green beam. Using an adaptive optics system prior to a lucky imaging detector, first tested in 2007 (Gladysz et al., 2007), allows obtain a higher number of images minimally affected by turbulence. The lucky imaging system averages the best images taken during the AO process to get a final image with higher resolution than it is possible with a regular long exposure AO camera. The EMCCD camera is an iXon 888 from Andor, with sensor diagonal size 18.8 mm and pixel size 13 μm.

3 WAVEFRONT SENSORS DESIGN

Throughout this section we will explain the design of each one of the wavefront sensors, at the concept level, the selection of the optical components as well as the outlook of the Slopes Calculation Program.

3.1 Shack Hartmann

In the operation of a wavefront sensor type SH there are three basic steps in the analysis process: determination of the spot positions, conversion to wavefront slopes, and the wavefront reconstruction.

In the design, the deformable mirror and the microlenses array (MA) are in a pupil conjugate plane, we are looking for the simplest setup, so our choice was to select a commercial MA. The first design was carried out using the MLA300-14AR(-M) Thorlabs model Square Grid with size 10mm x 10mm and lenslet pitch 300μm.

The higher the number of lenslets sampling the pupil, the higher is the spatial resolution of the measurements. However, this will lead to a lower signal to noise ratio since we reduce the amount of light by lenslet, so we have to find a balance between these two parameters. Our idea is to control the sampling varying the pupil size over the MA, and this is achieved by modifying the collimation lens that projects the pupil on the MA.

We need to know the minimum number of microlenses required to accurately sample the telescope's pupil. The seeing for a good night at the TCS in the Teide Observatory is $r_0 = 0.15m$. Therefore, the area of the telescope's pupil must be divided by the area of the atmospheric cell to know the regions in which our pupil has to be divided and, consequently, the minimum number of microlenses across our pupil:

$$\text{Number of regions} = \frac{(1.52)^2}{(0.15)^2} \sim 103 \text{ regions.}$$

Two different designs have been tested. The first one assumed a 5.4mm pupil, and therefore an oversampling of 20 x 20 microlenses. The results obtained both in laboratory and in the telescope are summarized in (Soria et al., 2020).

To improve the signal per microlense a second design was proposed. In this case we generate a pupil of 3.6 mm and therefore an sampling of 12 x 12 microlenses. The configuration of the detector camera is configured to read only the area in which the light falls, to reduce the sampling time.

A reference image whose spots falls in the centre of the microlenses areas is needed. To obtain this image, a reference beam is inserted placing an optical fiber in the focus of the telescope (Telescope Focus Figure 4). In this configuration, the only optical element that can introduce aberrations in the system is the DM, since without voltage the surface is not flat. For flattening, a commercial wavefront sensor (Thorlabs WFS40-7AR) placed after the collimating lens of the WFS beam. The readout has been connected to the control system and after the Static Characterization we have closed the loop and therefore the DM surface has been corrected until obtaining a flat wavefront. This flattening can be verified with the science image in the event that both optical paths are equal, if not, the dreaded Non Common Path Aberration (NCPA) will appear. This wavefront will be our objective readout throughout the test. This step is common for all the WFS.

3.2 Pyramidal

The operating principle of our Pyramidal WFS consist of focusing the distorted WF on the vertex of a pyramid by L1 and split into four beams by four facets of pyramid, and then four conjugated images of the pupil are produced on the detector camera by L2, see figure 2. I1, I2, I3 and I4 denote their respective intensity.

For the optical design, the *PAM2R.dll* dynamic linked library that define a user surface for ZEMAX has been used as a resource, describing a pyramid as an optical element for geometrical ray-tracing purposes developed by Arcetri (Antichi et al., 2016). One of the main problems in the manufacture of a pyramid by polishing is the roof-shaped tip, especially for small angles, which produce not evenly spread into four parts. The angle is limited by the area of the detector so two different pyramids have been proposed. A simple one with a base angle of 8 degrees, and a double one with 20 and 12 degrees. The use of a double pyramid allows to select a base angle greater than with a single pyramid configuration which results in an easier polishing process (Tozzi et al., 2008b). Nevertheless, because of the higher thickness, it creates another problem: the appearance of chromatic aberration. For this reason, a design with two different glasses is needed (Tozzi et al., 2008a). Both pyramids are still in the design process.

Due to the group's lack of experience with this sensor, the Slope Calculation Program will have to be developed. To date, the algorithm has been verified through different simulations, but it must be implemented in real time, and its output must be compatible with our Control Loop Program.

3.3 Two Pupil Plane Positions

This was the WFS used in the previous instrument AOLI. For this task, the optical design had to be changed because a much more compact instrument is needed, so to generate a sufficient difference in the optical path it was not possible to use a Lateral Prism. There are two Lateral Prisms available: 10mm and 20mm. The large one induces an excessive separation of the pupils on the detector, while the smaller one generates an optical path difference less than the depth of focus of the telescope, so the selected optical element to introduce the optical difference path is a pentaprism.

As we have mentioned, the greater the projection of the wavefront, the greater the resolution of our sensor, so the difference in the optical path that we introduce is proportional to it. This optical element induces two potential problems, the decrease in the intensity due to the absorption of the pentaprism and the inversion in the pupil. Therefore, some adjustments have been made in the slope calculation program. To solve the problem related to the differences in the illumination, it is carried out a normalization of each pupil, and for the inversion a X-flip is done in one of the pupils before applying the algorithm.
The steps to apply the Van Damm algorithm are explained in the simulation section. The real time SCP works in real time thanks to its GPU-accelerated implementation (Fernández-Valdivia et al. 2013)

4 PYTHON SIMULATIONS

We have been developing simulators for the 3 WFS to test the algorithm of each SCP. This study helps us better understand our system and be able to make sensor comparisons in a theoretical way. To carry out the simulations we used Python as programming language.

The setup components have been simulated using the High Contrast Imaging for Python (HCIPy) module developed by a group of astronomers at Leiden Observatory (Por et al., 2018), see table 1.

The phase profile of the deformable mirror $\psi_{DM}(x,y)$ can be described by two different ways: through a Gaussian profile of influence of each actuator c_{act} or set of modal functions $f_i(x,y)$ defined by:

$$\psi_{DM}(x,y) = \sum_i c_i f_i(x,y) \tag{1}$$

Modal reconstruction involves the estimation of the actuator state c_{act} or the modal coefficients c_i that compensate the incident aberration. Throughout this paper, the actuator modes will be used in Zernike mode.

For the reference image, the DM is flattened and a perfect flat wavefront that passes through the pupil of the telescope is generated. This WF passes through the different components, the pupil reducer, the DM and the different optical elements of each WFS, microlenses array (MA) for the SH, the pyramid for the PYR and 2 Fresnel propagator surfaces for the TP3. After that, the signal is read on the detector camera and the image is normalized. Once the camera is read out, each image is analysed though functions that carry out the algorithms explained in the section 3.

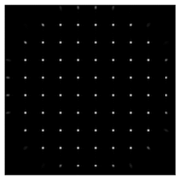

(a) Reference image for the SH.

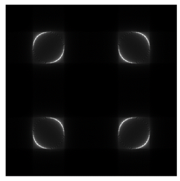

(b) Reference image for the Pyr.

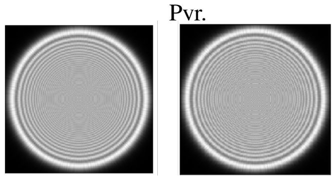

(c) Reference image for the TP3.

Figure 6: Reference image for each WF.

For the SH, the simulation of the MA is defined though the HCIPy function:

```
MicroLensArray(pup_grid,mla_grid,focal_length)
```

Where *pup_grid* defines the area in which the light will fall over the MA, *mla_grid* defines the positions of the centre of the micolenses, and *focal_length* is the value of the focal of the microlenses.

We use the reference image to select the lenslet area in which to measure each centroid (microlens pitch) and the ideal position of the spots, in the case of the simulation this points will be the same that the coordinates that define the pupil grid, see Figure 6a. To carry out this task we have implemented a function that from an input value of the spots distance, that we mark over the reference image, it performs a peak detection algorithm, and in the last iteration it saves the position of the centroid of each microlens and the parameter that characterize the readout area. This method allows us to apply the algorithm to different assemblies that we could use. From the reference we generate a mask that selects the areas of the detector in which the software has to measure the position of the centroids. To know which pixels we have to take into account, in this point, we apply a dynamic threshold which is proportional to the maximum pixel value in the cell. The localization of the spot behind each lenslet area is determined using a centre of mass algorithm. The x and y location are given by:

$$C_x = \frac{\sum_{i=1}^{N} x_i I_i}{\sum_{i=1}^{N} I_i}, \quad C_y = \frac{\sum_{i=1}^{N} y_i I_i}{\sum_{i=1}^{N} I_i}. \tag{2}$$

This calculus are involve in the following implemented function:

```
SH_estimator(det,regx,regy,regh,regw,refx,refy)
```

Table 1: Characteristics of simulated elements.

Parameter	Value
Telescope Diameter	1.5 m
Pupil diameter over the DM	18.11 mm
WFS Wavelength	700 nm
SH: Subapertures	12 x 12
SH: Focal	14.6mm
SH: Lenslet diameter	300 μm
Pyramid separation	0.04
TP3 optical path difference	10mm
DM: Actuators across pupil	9
DM influence	Zernike polynomails
Science camera	Noiseless detector 1024 x 1024 px
WFS camera	Noiseless detector 256 x 256 px
Number of Zernike reconstruct coefficients	30

Being *det* the image we want to process, and the rest of the inputs the parameters that mark the readout area.
From that moment, the SCP will measure the position of the centroids in each of the regions that we have defined on the detector and will compare the results with those of the reference image to calculate the displacements in x and y for each subaperture.

For the PYR WFS the pyramid is simulated though the HCIPy function:

```
PyramidWavefrontSensorOptics(pupil_grid,sep,wl_0)
```

Where *pup_grid* defines the area in which the light will fall, *sep*, separation, is related to the angle of the pyramid root, and *wl_0* is the wavelength used for sensing. To know the detector readout area, we have implemented a circle detection function:

```
Detect_circle(direction_image,minR,maxR)
```

Where *direction_image* point to the folder where the reference image has been saved, and *minR,maxR* delimit the expected range of the radius of the circle we are looking for in pixels. This function applied an Hough filter to the binarized reference image using the OpenCV library, and it returns the x and y coordinates of each detected circle and its radius. Using this parameters we could create a square mask that extract the pixel values of the detector which correspond to the pupils areas. To avoid edge effects, that we have verified to have a great weight in the reading of the WF, the readout area is 2 pixel smaller than the size of the detected circle. This approach allows operate with the pupils as simple matrices. Finally, we apply the algorithm to calculate the deviations in the x and y direction:

$$I_x = \frac{(I_a + I_b - I_c - I_d)}{norm} \tag{3}$$

$$I_y = \frac{(I_a - I_b - I_c + I_d)}{norm} \tag{4}$$

The normalization factor could be calculated using different methods (Bond et al., 2015). For this approach we have chosen the classical normalisation for a pyramidal WFS, a pixel-wise normalization. Every pixel intensity is normalised by the total intensity in that pixel position, summed across the four pupils. The algorithm has been implemented in the function:

```
Proc_pupil(aberr,pupils)
```

Where *aberr* is the detector frame that we want to analyse, and *pupils* contains the information regarding the areas of the detector that we have to read, namely, the output of the previous function Detect_circle.

In the case of the TP3 WFS, the optical path difference between the pupils has been generated adding to the beam two Fresnel surfaces defined in the HCIPy library:

```
F1=FresnelPropagator(pupil_grid,z,num_oversamp,n)
F2=FresnelPropagator(pupil_grid,-z,num_oversamp,n)
```

Once again *pupil_grid* marks the area in which the light will fall, *z* is half of the distance generated between the pupils, *oversamp* is the number of times the transfer function is oversampled, and *n* is the refractive index in which the light spreads. To simplify the process each pupil is read out in its own detector, so it is not necessary to extract the pupils. We use the reference image to delimiter the size of the pre-calculus polynomial slopes matrix and the coefficients read for the reference image are used as a baseline. Figure 6c. Following the Vam Dam article, the first step is to calculate the mean slope of the polynomials in the orthogonal direction to the projection. For every angle, α, and a circle of radius R this quantity is given by:

$$H_\alpha(u, Z_y) = \frac{1}{2\sqrt{R^2 - u^2}} \times \mathscr{R}\left(\frac{\partial Z_t(x,y)}{\partial x} cos(\theta) + \frac{\partial Z_t(x,y)}{\partial y} sen(\theta)\right) \tag{5}$$

Being $\mathscr{R}$ the Radon Transform and u the coordinates. The calculation of the Radon Transform has been implemented in python based on the code of Justin K. Romberg, making a small modification so that it returns the reference coordinates of the calculated sinogram, that we need to use in this algorithm. The derivatives of the Zernike polynomials can be computed directly from their mathematical definition. These calculations have been implemented within the following function:

```
H = g_wfs_precalc(modes, angles, x, y)
```

Whose inputs are *modes*, a vector with the modes used for the reconstruction, *angles* a vector with the projection angles for the Radon Transform, and the horizontal size, *x*, and vertical size, *y*, of the readout area. This function returns a 3D matrix H whose size is H[number of coords, number of angles, number of modes.

The Zernike coefficients a_i are then calculated through a least squares fit:

$$a_i = [H\alpha(u,Z_i)^T H_\alpha(u,Z_i)]^-1 H_\alpha(u,Z_i)^T p_\alpha(u) \quad (6)$$

Being $[H\alpha(u,Z_i)^T H_\alpha(u,Z_i)]^-1 H_\alpha(u,Z_i)^T$ the expression of the Moore-Penrose pseudo-inverse, a generalization of the inverse. The first step is to convert our 3D matriz in an 2D matrix to operate with it, for this task a simple reshape was applied. The second step is to carry out the pseudoinverse. To avoid degradation of the reconstruction by small singular values, we have used the Thicknov regularization that is implemented in the HCIPy library. We choose a tolerance of 10^{-3}.

The next step is to calculate the sinogram, by means of the Radon transform, of each of the unfocused pupils, and then relate the intensities by means of an histogram matching. Once I know the coordinates of each sinogram that have the same light intensity (u_1 and u_2), I can calculate the slope of the incident wavefront by:

$$\frac{\partial W}{r\partial u} = \frac{u_1 - u_2}{2 \cdot z} \quad (7)$$

Finally, to calculate the slope along the pupil we have to perform an interpolation of the measured values. The function chosen to carry out the interpolation has been *InterpolatedUnivariateSpline* from Scipy library. All these calculations have been implemented within the following function:

```
g_wfs(i1, i2, nangles, z ,H_pinv)
```

Where *i1* and *i2* are the detector images of each blur pupil, *nangles* the number of angles projected, z the distance in meters between each pupil and the pupil focus plane, and *H_pinv* the pseudo-inverse of the H matrix. This function returns the slopes calculated if H_pinv is NONE or otherwise the reconstructed Zernike coefficients.

Up to here we would have completed the simulation of the WFS module, the next phase will be the simulation of the calibration of our instrument.

For the linear reconstructor we need to now the Influence Matrix, which tells us how each wavefront sensor responds to each movement of the deformable mirror. We are working in Zernike mode basic for the DM characterization so the modal characterization can be build by sequentially applying a positive and negative single mode on the deformable mirror surface and reading the measurement on each WFS. The difference between the two WFS readouts gives us the DM response. The most common technique of wavefront reconstruction is to assume a linear relation between the measurement vector s and the modal coefficients c. The forward model is then given by:

$$s = M_{influ} \cdot c + N \quad (8)$$

Where M_{influ} is the Influence Matrix, s the WFS measurement, c the incoming perturbation and N some measurement noise from the WFS. The Influence Matrix can be calibrated by measuring the actuator response within the linearity range of the WFS. The inverse operation of reconstructing the WF from the slope measurements involves the estimation of the Actuation Matrix, M_{act}. This estimation requires inversion of the Influence Matrix. M_{influ} is not a square matrix so to apply the least-squares a pseudo-inverse in needed. Again we use the pseudo-inverse of Thicknov.

For each WFS we have implemented a function responsible of calculate M_{influ}. In addition to the requested parameters that characterize each WFS operation, there are some common inputs that indicates the number of DM actuators poke, the number of measurements and the number of modes that we apply to the DM.

Once we have completed the calibration process, we could reconstruct the shape of the incoming WF just multiplying the WFS lecture by the Actuation Matrix:

$$c = M_{act} \cdot s \quad (9)$$

4.1 Results

As our objective is to verify the reliability of the algorithm under different conditions, it is more useful to generate a controllable wavefront and check whether, after the analysis and reconstruction, the wavefront corresponds to the simulated one. It is a static measurement, so for simplicity we are going to resort leaving the deformable mirror in a random position and checking the reconstruction of its surface with each of the sensors. The results are shown in figures 7, 8 and 9:

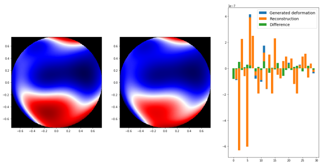

Figure 7: Reconstruction process for the SH module simulation.

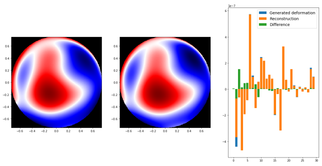

Figure 8: Reconstruction process for the TP3 module simulation.

The first image shows the DM surface when we send it a random signal, the second shows the reconstruction of the WF with each WFS, and the third figure shows an histogram with the generated modes (blue), the reconstructed modes (orange), as well as the difference between them (green).

On first thought, if we compare the first and the second figure, we see as the reconstruction algorithm used for the SH WFS and the TP3 WFS reconstruct the incident wavefront in a more faithful way than the algorithm used with the nm-PYR module showing the non-linear behaviour of this sensor referenced in the bibliography (Hutterer et al., 2019).
For a statistic study, we generate 90 random positions for the DM, working with 30 Zernike coefficient and leaving aside the mode 0 corresponding to the piston. Then, we perform the reconstruction process with each WFS and calculate the Root Mean Square (RMS) of the difference vector. Results obtained are summarized in table 2.

Table 2: Differences between the incoming WF and the reconstructed WF for each WFS.

	RMS (u.a.)
SH wfs	$(1.58 \pm 0.03) \cdot 10^{-02}$
Pyr wfs	$(2.1 \pm 0.6) \cdot 10^{-01}$
TP3 wfs	$(5 \pm 4) \cdot 10^{-02}$

In the absence of noise, the goodness of the reconstruction process differs by an order of magnitude between the PYR WFS and the others. SH WFS shows better results, with the smallest RMS. Moreover, the error associate to the RMS measurement indicates that the SH WFS is more precise.

To analyse the behaviour of the sensors under real conditions, we are going to carry out a study of the reconstruction process when the input signal is not clear. For this task we are going to add random noise to the detector camera, whose medium value is zero and the Standard Deviation (SD) will vary. This situation would reflects the observation with different reference stars magnitudes. The results in Figure 10 summarize the performance of the sensors, and error bars show the SD (over maximum and minimum values) of the measured RMS value for each noise value. See figure 10.

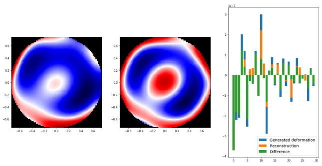

Figure 9: Reconstruction process for the Pyr module simulation.

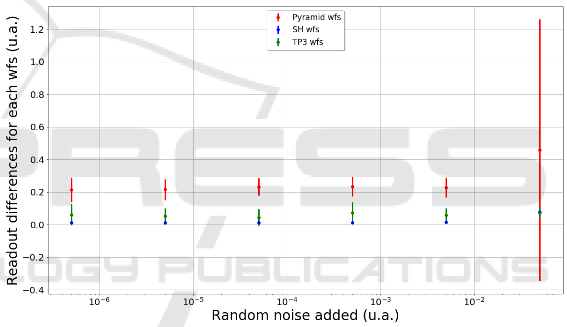

Figure 10: WFS response comparison for different SN ratios.

The same trend is followed when the measurements have noise. The high SD for the PYR WFS in the last point shows that this WFS is not capable of reconstruct the incident WF under this conditions while the SH and the TP3 get good results.

5 CONCLUSIONS

In the WFS comparison there are many requirements that we have to balance for the AO system design.

- Accuracy
- Efficiency (good use of photons)
- Speed (related with linearity)
- Robustness (chromaticity, ability to work on extended sources, etc ...)
- Other parameters (price, assembly-friendly..)

These simulations have given us the chance to test the implemented algorithm for the three WFS. Results show that the SH WFS is the most accurate and precise. The same efficiency has been obtained for the TP3 and the SH WFS.

Other requirements such as speed will have to be rated when the real time implementation will be finished for the three WFS. To compare others parameters specific test will be designed.

Furthermore, these simulations have allowed us to discard the nm-PYR for our instrument, opening the possibility of design a modulated one to increase linearity.

ACKNOWLEDGEMENTS

The research leading to these results received the support of the Spanish Ministry of Science and Innovation under the FEDER Agreement INSIDE-OOCC (ICTS-2019-03-IAC-12) and managed by the Instituto de Astrofísica de Canarias (IAC).

REFERENCES

Alejandro Oscoz, a. o. (2008). FastCam: a new lucky imaging instrument for medium-sized telescopes. In McLean, I. S. and Casali, M. M., editors, *Ground-based and Airborne Instrumentation for Astronomy II*, volume 7014, pages 1447 – 1458. International Society for Optics and Photonics, SPIE.

Antichi, J., Munari, M., Magrin, D., and Riccardi, A. (2016). Modeling pyramidal sensors in ray-tracing software by a suitable user-defined surface. *Journal of Astronomical Telescopes, Instruments, and Systems*, 2(2):1 – 7.

Bond, C., El Hadi, K., Sauvage, J. F., Correia, C., Fauvarque, O., Rabaud, D., Neichel, B., and Fusco, T. (2015). Experimental implementation of a Pyramid WFS: Towards the first SCAO systems for E-ELT. In *Adaptive Optics for Extremely Large Telescopes IV (AO4ELT4)*, page E6.

Colodro-Conde, C. and others. (2017). Laboratory and telescope demonstration of the TP3-WFS for the adaptive optics segment of AOLI. *Monthly Notices of the Royal Astronomical Society*, 467(3):2855–2868.

Colodro-Conde, C. and others. (2018). The TP3-WFS: a new guy in town. page arXiv:1811.05607.

Gladysz, S., Christou, J. C., and Redfern, M. (2007). “lucky imaging” with adaptive optics. In *Adaptive Optics: Analysis and Methods/Computational Optical Sensing and Imaging/Information Photonics/Signal Recovery and Synthesis Topical Meetings on CD-ROM*, page ATuA7. Optical Society of America.

Hickson, P. (2014). Atmospheric and adaptive optics. *The Astronomy and Astrophysics Review*, 22:1–38.

Hutterer, V., Ramlau, R., and Shatokhina, I. (2019). Real-time adaptive optics with pyramid wavefront sensors: part i. a theoretical analysis of the pyramid sensor model. *Inverse Problems*, 35(4):045007.

Por, E. H., Haffert, S. Y., Radhakrishnan, V. M., Doelman, D. S., Van Kooten, M., and Bos, S. P. (2018). High Contrast Imaging for Python (HCIPy): an open-source adaptive optics and coronagraph simulator. In *Adaptive Optics Systems VI*, volume 10703 of *Proc. SPIE*.

Ragazzoni, R. (1996). Pupil plane wavefront sensing with an oscillating prism. *Journal of Modern Optics*, 43(2):289–293.

Soria, E., López, R. L., Oscoz, A., and Colodro-Conde, C. (2020). ALIOLI: presentation and first steps. In Schreiber, L., Schmidt, D., and Vernet, E., editors, *Adaptive Optics Systems VII*, volume 11448, pages 517 – 525. International Society for Optics and Photonics, SPIE.

Thibos, L. N. (2000). Principles of hartmann-shack aberrometry. In *Vision Science and its Applications*, page NW6. Optical Society of America.

Tozzi, A., Stefanini, P., Pinna, E., and Esposito, S. (2008a). The double pyramid wavefront sensor for lbt. In Hubin, N., Max, C. E., and Wizinowich, P. L., editors, *Adaptive Optics Systems*, volume 7015, pages 1454 – 1462. International Society for Optics and Photonics, SPIE.

Tozzi, A., Stefanini, P., Pinna, E., and Esposito, S. (2008b). The double pyramid wavefront sensor for LBT. In Hubin, N., Max, C. E., and Wizinowich, P. L., editors, *Adaptive Optics Systems*, volume 7015, pages 1454 – 1462. International Society for Optics and Photonics, SPIE.

van Dam, M. A. and Lane, R. G. (2002). Wave-front sensing from defocused images by use of wave-front slopes. *Appl. Opt.*, 41(26):5497–5502.